

PAPER

Stress-dependent electrical impedance behaviours at fractal rough interfaces

To cite this article: Xu Wang *et al* 2021 *Surf. Topogr.: Metrol. Prop.* **9** 025014

View the [article online](#) for updates and enhancements.



IOP | ebooks™

Bringing together innovative digital publishing with leading authors from the global scientific community.

Start exploring the collection—download the first chapter of every title for free.

Surface Topography: Metrology and Properties



PAPER

Stress-dependent electrical impedance behaviours at fractal rough interfaces

Xu Wang¹ , Chongpu Zhai² and Yixiang Gan^{1,3}

¹ School of Civil Engineering, The University of Sydney, NSW 2006, Australia

² Hopkins Extreme Materials Institute, Johns Hopkins University, Baltimore, MD 21218, United States of America

³ The University of Sydney Nano Institute (Sydney Nano), The University of Sydney, NSW 2006, Australia

E-mail: yixiang.gan@sydney.edu.au

Keywords: electrical contact impedance, surface roughness, fractal dimension, insulating film thickness

Abstract

This work investigates interfacial electro-mechanical properties, including electrical contact resistance, interfacial capacitance and characteristic frequency of contacts formed with various surface structures. Fractal rough surfaces were generated and characterised by fractal dimension and root-mean-square (RMS) roughness. The rough surface with a thin oxide layer was compressed by the rigid flat to form a capacitor. Electrical impedances of this contact capacitor were simulated using the finite element method across a wide range of frequencies. A power-law relationship was found between the electrical contact resistance and applied compression load. An analytical model is proposed to capture the interfacial capacitance behaviour with increasing contact loads, revealing a transition of predominated modes for the capacitance. Higher fractal dimension yields smaller overall capacitance in the gap dominant and transition zones. The dependence of the characteristic frequency on compression was found to follow a power-law function at the low load range. It is found that the exponent and magnitude of obtained power-law relations show strong correlations to the fractal dimension and RMS roughness, respectively. Results of this work provide insights into developing a potential impedance measurement protocol to determine the thickness of the oxide layer on conductive fractal rough surfaces.

1. Introduction

Interfacial electro-mechanical behaviour plays an essential role in energy storage and transport systems such as lithium-ion batteries, solid oxide fuel cells and supercapacitors [1, 2]. The performance of these systems, represented by capacitance, is strongly affected by surface properties of contacting components, including electrical contact resistance [3], coating film thickness [4], bonding configuration [5], the fringing effect [6], and environmental conditions [7]. These parameters represented by the mechanical and electrical properties of granular electrode structure can be linked to microstructural characteristics, which are usually simplified in the existing theoretical and numerical models [8, 9].

The formation of an oxide layer on electrodes is reported to be the leading cause of electrical contact deterioration [4]. While performing measurements of the oxide layer on a naturally existing surface are still challenging to undertake. Several methods such as the

thermo-graphic method [10], optical method [11], and eddy current [12] have been adopted to investigate the properties of coating films, which usually require the coated surface to be adequately smooth and flat [10–12]. Being of considerable significance in fundamental research and engineering practices, the development of novel technologies for evaluating the thickness on both rough and flat thin film efficiently and accurately remains challenging.

Modelling conduction at rough interfaces under compression has attracted extensive and increasing interests since contact models by Greenwood *et al* [13, 14], followed by models [4, 15–17] with assumed surface roughness statistics and elastoplastic behaviour of individual asperities. Recent years also witnessed advances in understanding contact and conduction behaviour at rough interfaces with the development of novel numerical tools, such as studies on electrical conduction by finite element methods (FEM) [18], contact stiffness by boundary element method (BEM) [19], adhesion by molecular dynamics

(MD) [20], thermal conduction by FEM [21, 22]. However, scale-dependent electrical properties and multi-physic phenomena at interfaces bring numerical challenges in efficiently and precisely simulating electrical contact resistance at rough interfaces.

Pioneered by Dervos and Michaelides, the effective interfacial capacitance was found to depend on the ratio of the apparent contact area and true contact area, which is significantly smaller than the apparent one because of the nature of the multi-spot contact interface [23]. Zhao *et al* [24] theoretically studied the effects of interface roughness on the electric field and capacitance for capacitors formed by a thin insulating film. Kogut [8] investigated the effects of surface topography on the electro-mechanical characteristics of parallel-plate capacitors formed between hemisphere represented patterned surfaces. Patrikar [25] computed electrical parameters on 2D self-similar fractal surfaces for the application of capacitors by numerical methods. Yu *et al* [9] and Chen *et al* [26] modelled contact capacitors using rough surfaces with height and radius of asperities following Gaussian distributions. Torabi *et al* [27] extended the parallel-plate capacitor equation by Zhao [24] incorporating fractal surfaces described by roughness exponent, the root-

the oxide film thickness of both the FEM and analytical method are then compared in section 3.4. Section 3.5 provides the dependence of thickness electrical contact impedance on the thickness of oxide film on surface roughness. Finally, in section 4, we summarise the main findings and conclude this work. This study illustrates the essential prospects of a multi-physics understanding of the origin of the electro-mechanical behaviour at interfaces so that the performance and reliability of electrical contacts can be significantly improved in energy systems. Besides that, our work comes up with a new technique that is able to predict the oxide layer thickness of conductive rough surface by using impedance measurements of the interface. Comparing with the traditional approaches, the technique we proposed can remarkably reduce the sample preparation efforts and improve the measurement accuracy.

2. Methods

2.1. Surface generation and characterisation

Rough surfaces used to form contact capacitor are simulated by the modified Weierstrass–Mandelbrot function [28] written as

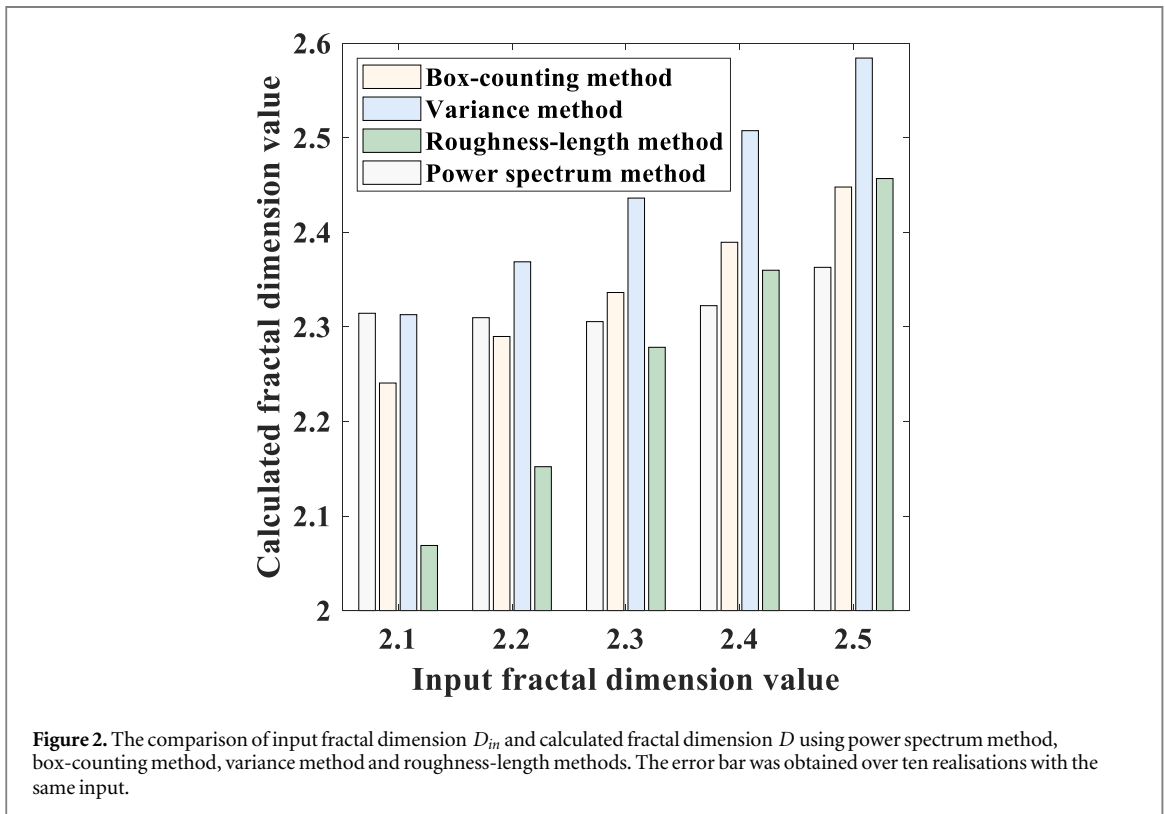
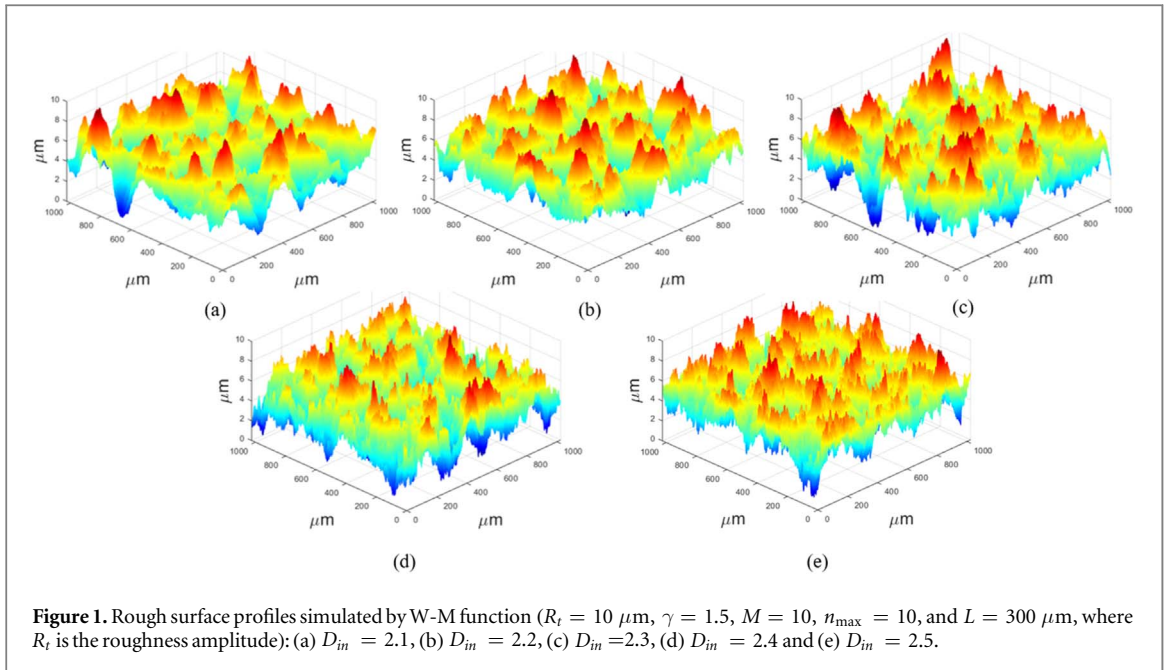
$$f(x, y) = L \left(\frac{G}{L} \right)^{(D_{in}-2)} \left(\frac{\ln \gamma}{M} \right)^{\frac{1}{2}} \sum_{m=1}^M \sum_{n=0}^{n_{\max}} \gamma^{(D_{in}-3)n} \times \left\{ \cos \phi_{m,n} - \cos \left[\frac{2\pi \gamma^n (x^2 + y^2)^{\frac{1}{2}}}{L} \cos \left(\tan^{-1} \left(\frac{y}{x} \right) - \frac{\pi m}{M} \right) + \phi_{m,n} \right] \right\} \quad (1)$$

mean-square roughness (R_{RMS}) and correlation length. Though capacitance of rough interfaces has been extensively studied, the capacitance evolution at the rough surface under compression and the presenting features of electrical contact impedance in frequency domains necessitate further investigations.

In this work, we developed an analytical solution for obtaining the interfacial capacitance under the mechanical compression, and validated by the FEM simulation. In addition, an innovative approach was proposed to estimate the oxide film thickness using the electrical contact behaviours. In section 2, we present the numerical framework used in this work for generating rough surface and estimating the contact behaviour, for both mechanical and electrical responses. The modified Weierstrass–Mandelbrot function is adopted for generating fractal rough surfaces, characterised by four methods regarding fractal dimension. The contact mechanics is extracted by the truncation method, and the electrical behaviours of the surfaces in contact are investigated by FEM. The effects of surface roughness on electrical behaviours are demonstrated in sections 3.1 and 3.2. Section 3.3 describes the derivation of the analytical model for stress-dependent interfacial capacitance. The effects of

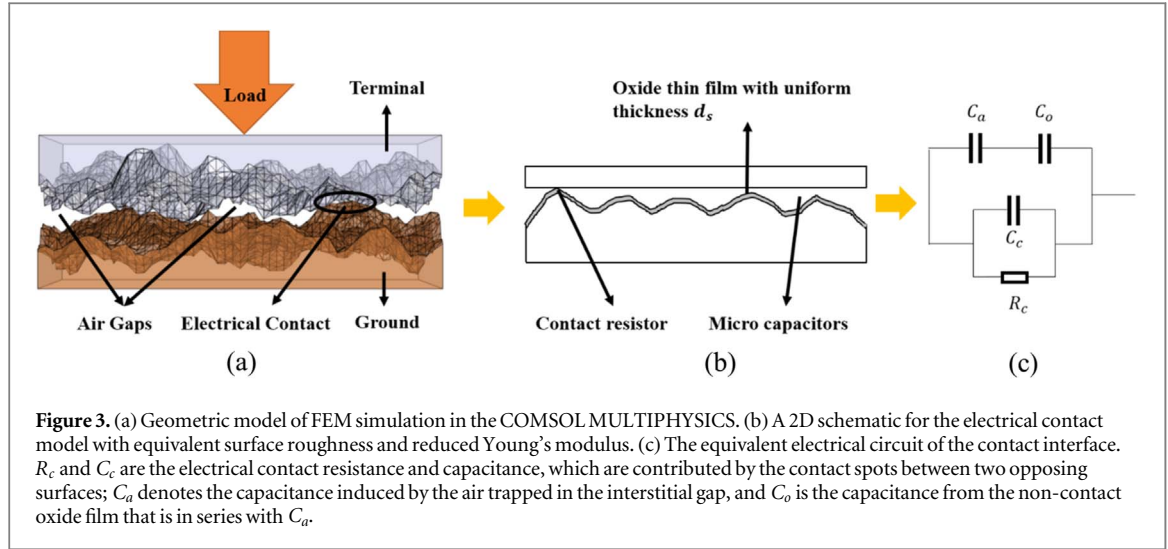
where L represents the sample length, G is the fractal roughness [29], which is a height scaling parameter independent of the frequency. D_{in} is the fractal dimension ranging from 2 to 3. A higher value of D_{in} results in a rough surface with the structure dominated by high-frequency textures. The parameter γ determines the density of frequencies to construct the surface profile, which is set here as 1.5 after considering surface flatness and frequency distribution density [30]. The factor M is the number of superposed ridges that used to construct the surface profiles, n_{\max} represents the upper bound of frequency index that can be determined by ($n_{\max} = \text{int}[\log(L/L_s) / \log \gamma]$), L_s and L are the cut-off length and roll-off wavelength, respectively [31], and $\phi_{m,n}$ is a set of randomly distributed phase angles to ensure the randomness.

Figure 1 shows five surfaces with 1024×1024 pixels over $1 \times 1 \text{ mm}^2$ with the same roughness amplitude and roll-off wavelength but different values of fractal dimensions, demonstrating distinguished structures especially at fine length scales, contributed by high-frequency components. In this work, we considered surfaces structures with $D_{in} < 2.5$, considering that the fractal dimension for engineering surfaces are typically under 2.5 [32].



The input parameter fractal dimension D_{in} was found not necessarily an accurate evaluation of the generated rough surface profile [33]. Hence, four widely-used methods are adopted here to estimate the value of fractal dimension for generated rough surfaces including (1) power-spectrum method [34], (2) box-counting method [35], (3) variance method [36, 37] and (4) roughness-length method [38]. Values of fractal dimension calculated based on these four methods were found to be slightly different, but following the same trend, i.e., a higher D_{in} resulted in a

higher evaluated value, as is shown in figure 2. It is found that differences are relatively small between the input parameter D_{in} and the fractal dimension estimated by the roughness-length method. Despite the results of the power spectrum method, the rest results predicted by the other three methods highlight that the trend of output fractal dimensions are consistent with the input parameter D_{in} . Besides the fractal dimension, the conventional roughness parameter, the root-mean-square roughness, R_{RMS} , was used to characterise surface structures, calculated as :



$$R_{RMS} = \sqrt{\frac{1}{N \times N} \sum_{x=1}^N \sum_{y=1}^N (f(x, y) - \bar{f})^2}, \quad (2)$$

where N is pixel number on a profile along either X and Y -axis, \bar{f} is the mean roughness height over all pixels calculated based on equation (1). Desired roughness amplitude R_t can be obtained by scaling the roughness amplitude $(f(x, y) - \bar{f})$ for self-similar rough surfaces [30].

2.2. Contact model

As a conventional method in contact mechanics, two rough surfaces in close contact (figure 3(a)) can be considered as equivalent to a system of a rigid flat surface compressing a rough surface (figure 3(b)) with a reduced Young's modulus $E_r = \left[\frac{1 - \nu_1^2}{E_1} + \frac{1 - \nu_2^2}{E_2} \right]^{-1}$, where ν_1 , E_1 , ν_2 and E_2 are the Poisson ratio and Young's modulus of the compressed rough surface and opposing flat surface. Therefore, the study investigates the contact electrical behaviours between two rough surfaces are represented by the same equivalent system where a rough surface covered by a thin oxide layer is compressed by a rigid flat.

Since the main objective here is to reveal the electrical behaviour of rough interface during surface contact, the contact model is simplified in order to achieve computational efficiency. Therefore, the truncation contact model [30] is adopted here to capture the contact behaviours between the surface compression process. In the truncation model, the contact area was estimated by the truncation area as the surface approaching. During the flattening processing, the corresponding contact stiffness at each truncation stage is updated based on [39]:

$$k = \beta \frac{2}{\sqrt{\pi}} E_r \sqrt{A_c} \quad (3)$$

where k is the contact stiffness with the unit of N/m , β is a geometrical constant, set as 1 for a flat punch [30]. E_r denotes the reduced Young's modulus introduced

above. A_c is the real contact area at each truncating step, which equals to the area was flattened by the flat rigid surface. An integration with respect to flatten increment is applied in order to carry out the contact force, based on $dF = k(\omega)d\omega$, where $d\omega$ denotes the interference increment. The adopted method provides an easily incorporated and highly effective numerical method for predicting contact stiffness under conditions of small to medium loads for a single asperity and fractal rough surfaces. For a fractal rough surface compressed by a rigid flat, the numerical solution with this method for contact stiffness versus contact load well agrees with the classical theory result. However, as the compression and truncation depth increase, the applicability of the presented method merits further discussion, due to the complex deformation of the compressed asperities, the interaction between neighbouring asperities, adhesion, and friction [30]. Therefore, the applied compression is constrained to a level of $\frac{F}{EA} < 10^{-2}$ and the overall compression depth δ_{\max} is limited to $0.3 R_t$ in this work. Furthermore, the penetration increment is considered as $d\omega \ll \delta_{\max}$ to achieve validity and computational efficiency. In addition, for simplicity, the oxide layer covered on the surface has similar properties as the bulk and is assumed to keep intact during the different loading process. More details regarding this adopted contact model can be referred to Ref [30]. Note that, the oxide layer on the surface has similar properties as the bulk and is assumed to keep intact during different loading process for simplicity. However, future work should address the fracture effects of the oxide layer under permanent deformation, which can be achieved by explicitly simulating the coupled mechanical and electrical properties of the oxide layer.

2.3. Interfacial impedance responses

The electrical impedance responses were considered as a conductive rigid flat in contact with a fractal rough surface covered by an oxide layer of uniform thickness since the previous contact model simplification, as illustrated in figures 3(a) and (b). The top surface of

the rigid flat was set as the terminal electrode with a controlled alternating voltage. While the compressed rough surfaces were generated using the modified Weierstrass–Mandelbrot function (see section 2.1) and the bottoms of the samples were set as ground with the electric potential of 0. The conductive rough surface was covered by an oxide layer of a given thickness $d_s = 100$ nm [40–42], as a typical value for copper oxide films varying from 40 nm to 450 nm. Due to the conductivity contrast between the oxide layer and bulk material, the thickness of the samples has negligible influences on the overall behaviour. For a rough surface with given values of fractal dimension and R_{RMS} , ten typical truncation planes at various depths with the same height intervals ($0.03R_t$) were simulated to obtain their electrical impedance, during the compression process.

The complex electric field, current and potential distributions of the conducting rough surfaces were governed by the following equations (4)–(7):

$$\nabla \cdot J = Q_{j,v} \quad (4)$$

$$J = (\sigma + j\omega_a \varepsilon_0 \varepsilon_{rc}) E_e + J_e \quad (5)$$

$$E_e = -\nabla V \quad (6)$$

$$D = \varepsilon_0 \varepsilon_{rc} E_e \quad (7)$$

where J and J_e denote the internal and external current density, σ is the electrical conductivity of copper, E_e is the electric field intensity, V is the electric potential, D is the electric displacement, ε_0 and ε_{rc} are the permittivity of vacuum and the relative permittivity of copper, respectively, and ω_a is the angular frequency $\omega_a = 2\pi f$. Here, the inductive effects were negligible, considering the system dimensions. The oxide layer on the rough surface was modelled as an insulative material with the electrical response in the frequency domain governed by:

$$n \cdot J_1 = \frac{1}{d_s} (\sigma_o + j\omega \varepsilon_0 \varepsilon_{ro}) (V_1 - V_2) \quad (8)$$

$$n \cdot J_2 = \frac{1}{d_s} (\sigma_o + j\omega \varepsilon_0 \varepsilon_{ro}) (V_2 - V_1) \quad (9)$$

where J_1 , J_2 are the current density of two sides of an oxide film; d_s denotes the surface thickness of the modelled boundary elements; σ_o and ε_{ro} are the electrical conductivity and relative permittivity of the oxide film; j is the dimensionless imaginary unit.

The electrical impedance spectra of the contact and the current flow through the rough interfaces were then simulated by the commercial finite element method (FEM) package, COMSOL Multiphysics version 5.3a. The total current flowing from the rigid top flat (terminal electrode) to the compressed rough surface (the ground electrode) was obtained by integrating the current density across the interface. Therefore, the effective admittance, Y , can be determined by using the applied voltage and integrated total current density. The electrical contact resistance (ECR) and interfacial capacitance (C) can be calculated from the

Table 1. Geometrical and physical parameters of the three-dimension fractal rough samples and the oxide layer used in numerical simulations [40, 41, 43–45].

Parameters	Value
Dimensions of compressed surface (μm^2)	256×256
Permittivity of air, ε_0 ($\frac{\text{F}}{\text{m}}$) (–)	8.854×10^{-12}
Electrical conductivity of copper, σ (S/m)	5.998×10^{-7}
Relative permittivity of copper, ε_{rc} (–)	1
Elastic modulus of copper, E (GPa)	128
Thickness of copper oxide layer (nm)	100
Electrical conductivity of oxide layer, σ_o (S m^{-1})	0.01
Relative permittivity of the oxide layer, ε_{ro} (–)	25
Poisson's ratio, ν (–)	0.3
Yield strength of copper, G (MPa)	210

impedance, Z . The following expressions show their relationship:

$$Z = \frac{1}{Y} = Z' + Z''j \quad (10)$$

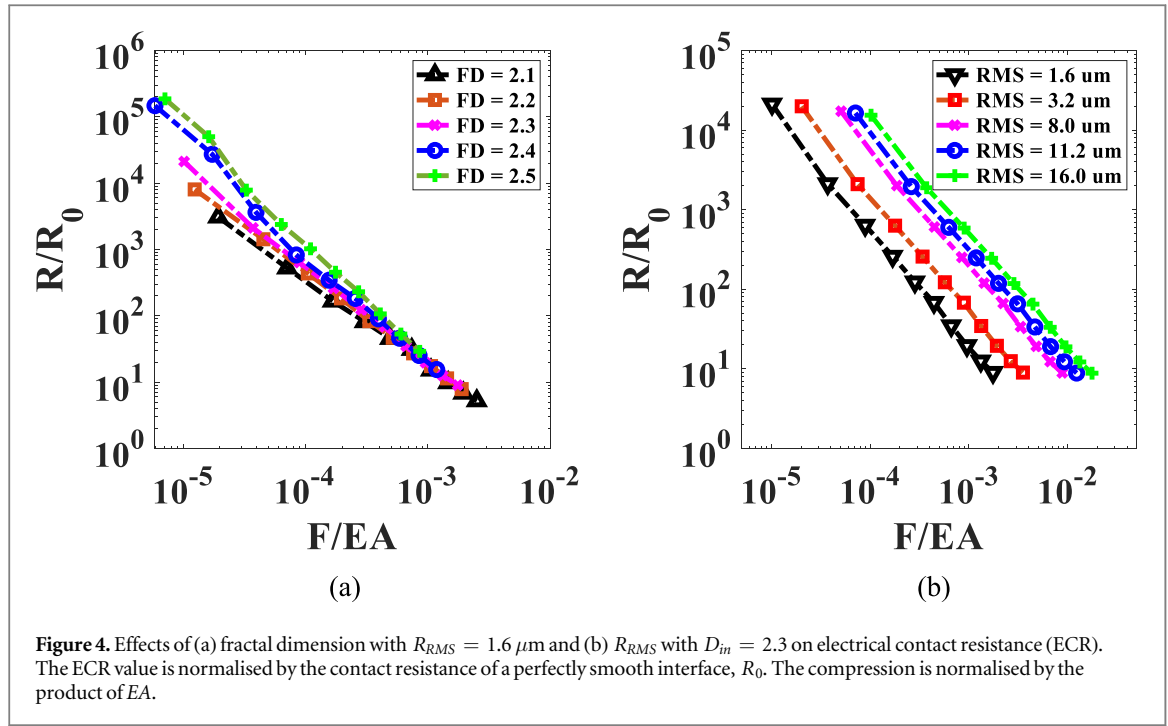
where Z' and Z'' denote the real and imaginary parts of the complex impedance. The ECR values can be obtained as the real part of the interfacial impedance, while the capacitance is calculated by an encompassing electrostatic formula, i.e., $C = \text{Im}(Y(\omega))/\omega$, where $Y(\omega)$ is the interfacial admittance, and ω is the angular frequency.

The electrical contact impedance of a series of compressed surfaces is simulated with a fractal dimension of $2 < D_m \leq 2.5$ and R_{RMS} of $1.6 \mu\text{m} \leq R_{RMS} \leq 16 \mu\text{m}$ and apparent projection area of $256 \times 256 \mu\text{m}^2$. Geometrical (fractal dimension, R_{RMS} can be included in the table) and physical parameters used in simulations are listed in table 1. A mesh sensitivity study has been performed to ensure the electrical impedance converges to an asymptotic value. In this work, the mesh comprises 735,362 tetrahedral elements. The minimum mesh elements concentrate at the local roughness asperities have a size of $2.55 \mu\text{m}$ enabling computing the interfacial electrical behaviours accurately (the difference between the results of the selected mesh sizes and the extremely fine mesh is within 5%).

3. Results and discussion

3.1. Electrical contact resistance

Results are demonstrated for various roughness parameters to reveal the effects of surface topographies on ECR in figure 4. To examine the effects of the scale-invariant parameter, the fractal dimension varies in the range of $2.1 \leq FD \leq 2.5$ whilst the RMS roughness was fixed ($RMS = 1.6 \mu\text{m}$). Figure 4(a) shows the dependence of ECR on fractal dimension and normalised applied force for fixed RMS roughness. The ECR decreases with the increase of applied contact load due to the increase of the true contact area during the surface compression process, while for a fixed contact



load, the contact area is larger for the surface with smaller fractal dimension, therefore, decreases the ECR. As predicted, smaller fractal dimension values corresponding to a smoother surface profile, leading to a larger true contact area and hence a lower ECR. It is worth to mention that the slope for each curve, at the log-log space, with varying fractal dimension is different, rougher surface with higher fractal dimension shows a greater slope. This is because the correlation between the contact area and contact load for the fractal rough surface is a power-law relationship, and the power exponent is positive proportion to the fractal dimension [5, 19, 46]. The ECR values are not distinguishable for surfaces with different fractal dimensions when the non-dimension contact load, F/EA , is large than 10^{-3} . The reason is that the majority of microcontacts are deformed fully plastically, and the ECR values become independent of the surface topography parameters [4], in other words, the contact behaviour is insensitive to the initial fractal dimension when the contact loading is extensive.

To further elucidate the role of rough topography, the effects of RMS roughness was studied. Figure 4(b) illustrates the dependence of ECR values concerning contact load and RMS roughness for the fractal dimension $FD = 2.3$. For a fixed fractal dimension value, the ECR is decreasing with the increase of contact load since the contact area increases as well, whereas, for a fixed contact load, the ECR increase with RMS roughness values due to more considerable RMS value corresponding to the rougher surface, producing smaller contact area at the same contact force.

The ECR for different fractal dimension shows a converging trend as the compression increases. For a given D_m at a fixed compression level, ECR was found

to increase with R_{RMS} , which tend to play a minor role on the slope of power-law dependence of ECR on compression. These relationships can be then described by:

$$R = \frac{1}{\sigma_o} \frac{d_s}{A_c}, \quad A_c \propto \alpha_c \left(\frac{F}{EA} \right)^{\beta_c} \quad (11)$$

where σ_o and d_s are the electrical conductivity and thickness of oxide film, and A_c is the true contact area, α_c and β_c are the parameters obtained by correlation analyses for ECR of various surface roughness. This relationship between α_c , β_c and D_m , R_{RMS} are extensively investigated by previous studies [5, 19, 46], which shows the relation between the constriction conductance and compression force of contact of two surfaces. The slope and intersect parameters α_c (in equation (11)) and β_c can be affected by the mechanical properties of contact material such as Young's modulus E and yield stress G . In the current simulation, the material mechanical properties are considered by the contact model (i.e., truncation method) regarding the conversion from contact area to contact force. Considering silver as a replacement material, for example, different combinations of Young's modulus and yield stress can be applied in the truncation contact model, leading to a similar power-law relationship but with distinctive slope β_c and intersect α_c . Table 2 summarizes the coefficients fitted based on the dataset from figure 4(a) for a given R_{RMS} value, to show the dependences on the fractal dimension. These results also indicate that the *in situ* ECR measurements can be used to identify the metallic contact conditions since they are sensitive to the surface roughness and the contact information [47].

Table 2. Fitting parameters of α_c and β_c with respect to the rough surfaces with varying fractal dimension and a fixed R_{RMS} (1.6 μm).

Fractal dimension	α_c	β_c	R-Square
2.1	-6.136	-1.301	0.9971
2.2	-6.700	-1.394	0.9999
2.3	-6.956	-1.438	0.9993
2.4	-8.860	-1.699	0.9911
2.5	-9.455	-1.806	0.9948

3.2. Interfacial capacitance

The dependence of interfacial capacitance on roughness parameters was examined, and the results are shown in figure 5. A clear stress-dependent transition can be observed as the compression increases. The interfacial capacitance is contributed by both air gap and micro-contacts on oxide, dominating the capacitance at low and high loading levels, respectively, as is discussed in section 3.3.

The results shown in figure 5(a) describe the effects of scale-invariant fractal parameters on the interfacial capacitance under varying contact load. For fixed D_{in} , the interfacial capacitance increases with increasing of contact load due to the decrease of the distance of the air gap and the excess capacitance produced by the oxide layer with increasing contact area. Moreover, as shown in the insertion of figure 5(a), the slope for interfacial capacitance variation decreases with increase with D_{in} . For fixed contact load, the interfacial capacitance is decreasing with the increase of fractal dimension when the dimensionless contact load is at lower to intermediate contact loading regime ($\frac{F}{EA} < 10^{-4}$). However, the differences in interfacial capacitance with various fractal dimension are relatively small when the contact load get even more significant. This is because the capacitance at the high contact load level is dominant by the capacitance produced by the contact oxide film, which is illustrated in the later section 3.3. At the same time, the fractal dimension is not capable of distinguishing the contact behaviours at that contact load range. Nevertheless, the slope of capacitance versus contact load curves at a higher contact range is still different for various fractal dimension, and a higher fractal dimension yields a higher slope for the capacitance evolution. These results coincide with the previous study regarding contact stiffness of fractal rough surface [48].

Figure 5(b) presents the relationships between interfacial capacitance and contact load with the change of R_{RMS} (1.6 $\mu\text{m} \leq R_{RMS} \leq 16 \mu\text{m}$). It can be observed that the R_{RMS} roughness has a more significant effect on the interfacial capacitance over the fractal dimension. For a fixed contact load, the interfacial capacitance decreases with increasing the R_{RMS} parameters due to the increase of gap distance and the decrease of the true contact area. Since higher R_{RMS} values are corresponding to rougher surfaces, yielding

more considerable gap distance and smaller true contact area and, thus, smaller interfacial capacitance.

In addition, regardless of the interfacial capacitance is increasing with the applied contact load, it is noted that the rates of increase with respect to given contact load are different, and the increasing rate is small at a low to intermediate contact load, while this rate is keeping increase as the contact load increases, and it will end up with a constant when the contact load is sufficiently large. This is because the total interfacial capacitance is contributed by two components: capacitance from gap and contact oxide layer [9, 26]. Those two components both vary with the increase of contact load since the gap distance between two surfaces is getting smaller, whilst the true contact area keeps increasing. Therefore, the overall trend of capacitance variation can be explained; the total capacitance is dominant by the contribution from the gap capacitance under low contact load, this is why the increase rate is low at the beginning since the gap distance variation is relatively small. As the contact load getting higher, the increase rate accelerates due to the contact capacitance is getting larger that is compatible with the gap capacitance. Eventually, the contact capacitance will be significantly higher than the gap capacitance, and dominant the overall behaviours. Base on the above mechanism, we derive an analytical model to predict the interfacial capacitance during the contact processing, and the detailed demonstrations are given in the later section.

3.3. Analytical model for stress-dependent interfacial capacitance

As discussed in the previous section, the total effective contact capacitance of the studied interface can be expressed as:

$$C_t = C_c + C_g \quad (12)$$

where C_c is the capacitance contributed by all the microcontacts, calculated by the classical parallel capacitor equation, $C_c = \sum_{i=1}^n c_{ci}$, with the capacitance of each microcontact calculated by $C_{ci} = \frac{\epsilon_r \epsilon_0 A_c}{d_i}$, where ϵ_r and ϵ_0 denote the relative permittivity of the oxide layer and absolute permittivity of vacuum, respectively. Here, A_c is the true contact area at a given contact load, which is accessible in our contact analysis, and d_i is the thickness of the oxide layer.

The capacitance C_g is the gap capacitance that accounts for non-contacting regions at the interface, it can be considered as the capacitance induced by the air gap in series with capacitance due to oxide layer:

$$\frac{1}{C_g} = \frac{1}{C_a} + \frac{1}{C_o} \quad (13)$$

where C_a and C_o are the capacitance contributed by air and non-contact oxide layer respectively. The capacitance of the non-contact oxide layer C_o can be obtained as a rough capacitor with uniform inner distance d_s , for given surface structures, as:

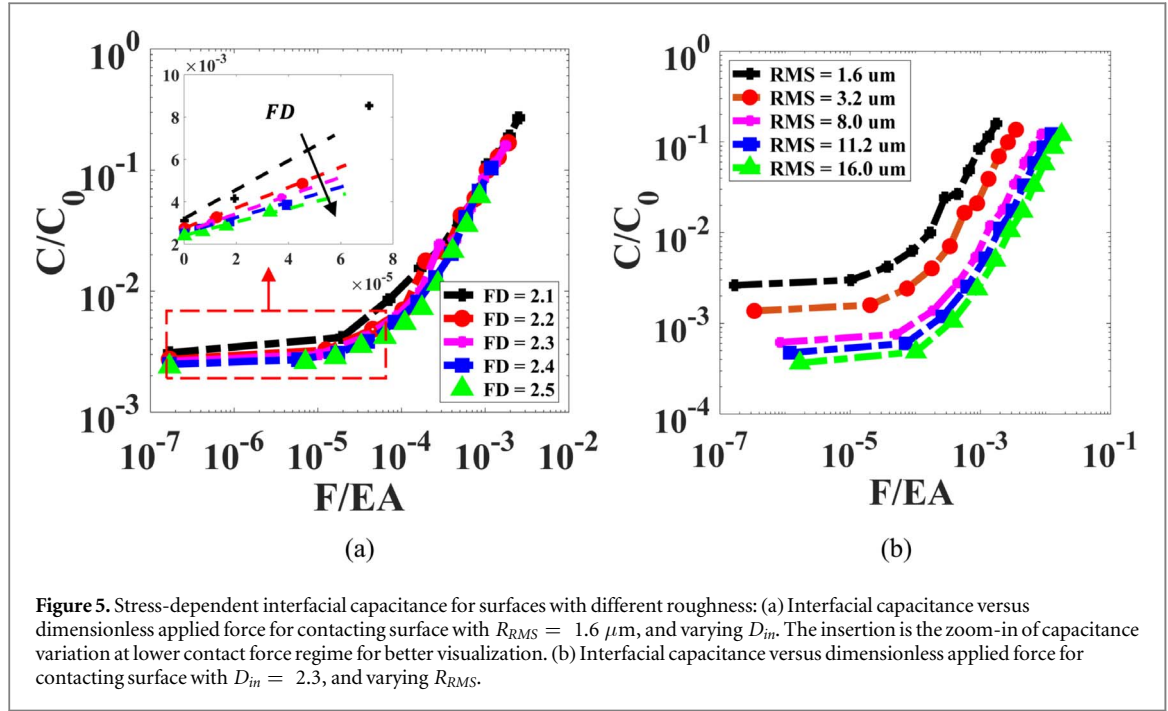


Figure 5. Stress-dependent interfacial capacitance for surfaces with different roughness: (a) Interfacial capacitance versus dimensionless applied force for contacting surface with $R_{RMS} = 1.6 \mu m$, and varying D_{in} . The insertion is the zoom-in of capacitance variation at lower contact force regime for better visualization. (b) Interfacial capacitance versus dimensionless applied force for contacting surface with $D_{in} = 2.3$, and varying R_{RMS} .

$$C_o = \frac{\varepsilon_r \varepsilon_0 (A_t - A_c)}{d_s} \cong \frac{\varepsilon_r \varepsilon_0 A_t}{d_s} \quad (14)$$

where A_t is the total area of the rough bottom surface. Since the real contact area is significantly small compared to the apparent contact area [49] ($A_t \gg A_c$), the term of contact area (A_c) can be neglected ($A_t - A_c \cong A_t$). Thus, the equation of non-contact oxide layer capacitance (equation (14)) is simplified. However, it is difficult to determine the actual capacitance resulted from the air gap due to the existence of the roughness textures. We assume that the overall capacitance is composed of infinite small micro capacitors connected in parallel with various separate distances. The capacitance for the infinitesimal capacitor can be expressed as:

$$dC = \frac{\varepsilon_0 dA}{d_t - Z_i} \cong \frac{\varepsilon_0 dA}{R_t - Z_i} \quad (15)$$

R_t denotes the roughness amplitude that is the distance between the peak and valley of surface topography, and $f(x, y)$ is the surface profile ($f(x, y) \in [0, R_t]$), and d_t is the height of terminal, which approximate as roughness amplitude (R_t) when the contact force is relatively small, leading to the expression on the right side. Hence, the total capacitance contributed by air can be calculated by treating these micro capacitors as parallel plate capacitors, calculated as:

$$C_a = \int_0^A \frac{\varepsilon_0}{R_t - f(x, y)} dA. \quad (16)$$

It is found that the capacitance contributed by the air gap is dramatically smaller than that of the non-contact oxide layer, thus, its reciprocal dominating the overall contact capacitance. The non-contact oxide layer capacitance term can be neglected according to equation (15), yielding the approximated total

capacitance expression:

$$C_t = \frac{\varepsilon_r \varepsilon_0 A_c}{d_s} + \int_0^A \frac{\varepsilon_0 dA}{R_t - Z_i}. \quad (17)$$

Figure 6 illustrates the comparison between simulated dimensionless capacitance and analytical results from the previously introduced model with varying R_{RMS} . The analytical model prediction and numerical simulation results show a good agreement, validating the proposed analytical model in the previous section. There are three regimes dominant the stress-dependent interfacial capacitance on fractal rough surfaces: (1) capacitance from air gap dominant as contact load is low, (2) transition zone that the magnitude of the gap and contact capacitance are compatible when the contact load is low to intermediate, and (3) contact capacitance dominant under large contact loads. Based on the proposed analytical model, we are able to predict the contact-induced interfacial capacitance for given surface topography. It is interesting to note that, for smaller R_{RMS} , the prediction from the analytical model is slightly smaller than the simulation results; this is due to the neglected contribution from non-contact oxide layer capacitance, yielding a slight underprediction.

3.4. Effects of oxide film thickness on interfacial capacitance

The role of oxide layer thickness on stress-dependent capacitance was evaluated by a further parametric study. As is shown in figure 7, the transition point tends to appear at high compression for cases with a thicker oxide layer. This trend can be potentially used to determine the oxide layer from the measurements of contact load and interfacial capacitance, provided surface topographies are known.

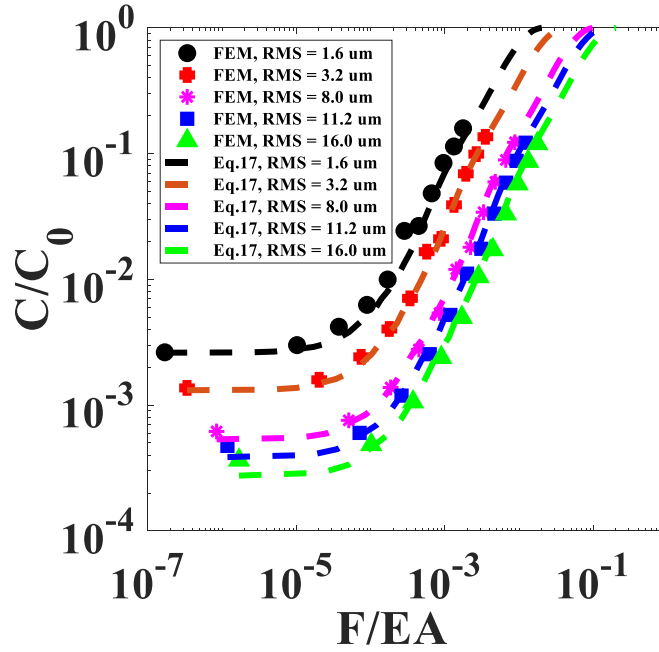


Figure 6. Comparison of the analytical solutions and FEM simulations for the interfacial capacitance of surfaces with $D_m = 2.3$ and various R_{RMS} . Scatter points show the FEM simulated capacitance, and the dashed lines represent the analytical model predictions. Note that the colour of FEM simulation and derived model results for the same surface parameter is the same for the reason of comparison.

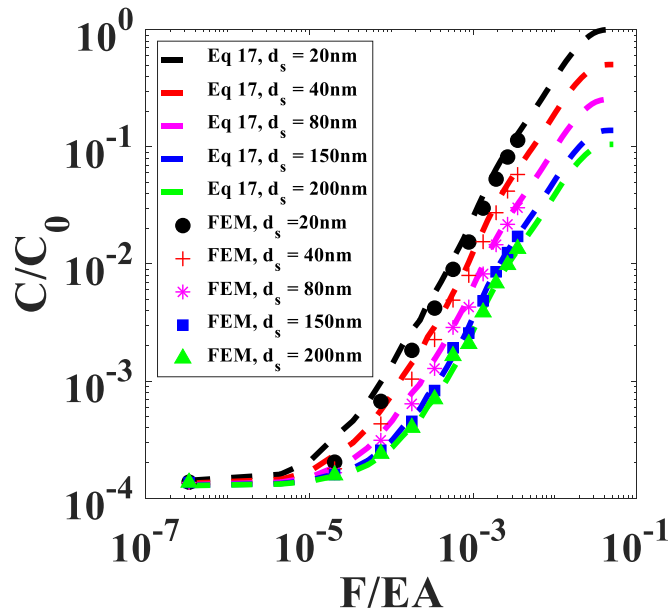


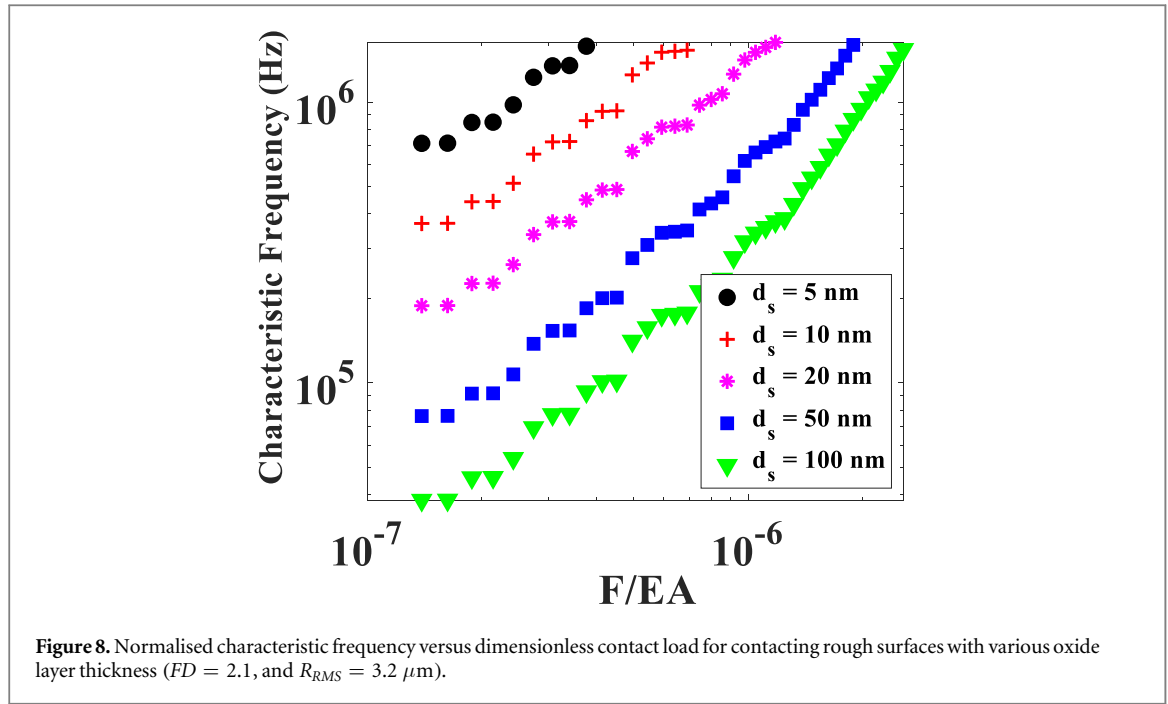
Figure 7. Normalised interfacial capacitance versus dimensionless contact load for contacting rough surfaces with various oxide layer thickness ($FD = 2.3$, $RMS = 3.2 \mu m$). Scatter points indicate the capacitance from FEM simulations, while the dash lines represent the prediction by the analytical model. Note that the colour of FEM simulation and derived model results for the same surface parameter is the same for the reason of comparison.

3.5. Characteristic frequency with the presence of oxide film

It is necessary to know the entire surface topology in order to obtain the thickness of the oxide layer from the stress-dependent expression of interfacial capacitance shown in equation (17). This process is iterative and tedious to measure the surface topology after each increment of contact load and impedance analysis.

However, characteristic frequency plays an essential role in studying the behaviours of the interface, which has the advantage that is easy to measure, and correlates with both stress-dependent electrical restriction resistance R and interface capacitance C as well.

The characteristic frequency is defined as the frequency that the real part of impedance equals the



imagining part of impedance during the frequency spectrum. For the interface that we are interested in, an RC parallel circuit can be considered as an equivalent circuit model [7, 50, 51], shown in figure 3. Therefore, the equivalent impedance can be calculated as:

$$Z = \frac{R}{1 + j\omega C} \quad (18)$$

Here Z is the equivalent impedance, R and C denote electrical constriction resistance and interfacial capacitance for a given load, respectively, and ω is the angular frequency that can be determined by ordinary frequency: $\omega = 2\pi\tau$. Thus, the characteristic frequency of the equivalent circuit can be expressed as:

$$\tau = \frac{1}{2\pi CR} \quad (19)$$

The characteristic frequency is determined by the product of resistance R and capacitance C . Since the interfacial capacitance shows a non-linear relationship with increasing contact load, it will alter the behaviour of characteristic frequency under the surface contacting. By substituting equations (11) and (17) into equation (19), the variation of characteristic frequency with increasing of contact load can be determined, yielding the expression:

$$\tau = \frac{1}{2\pi \left(\varepsilon_r \varepsilon_0 \rho + \rho \frac{d_s}{A_c} \int_0^A \frac{\varepsilon_0}{R_t - Z_i} dA \right)} \quad (20)$$

It is interesting to point out that the characteristic frequencies for varying oxide layer thickness cases are converging to a specific frequency as the contact load increasing, this is because the interfacial capacitance is dominant by the capacitance from the contact oxide layer at high contact load. Therefore, the term determines gap capacitance in equation (20) can be

Table 3. Fitting parameters of α_τ , β_τ and R-Square with respect to the rough surface with fractal dimension ($D_{in} = 2.1$) and fixed R_{RMS} ($1.6 \mu\text{m}$).

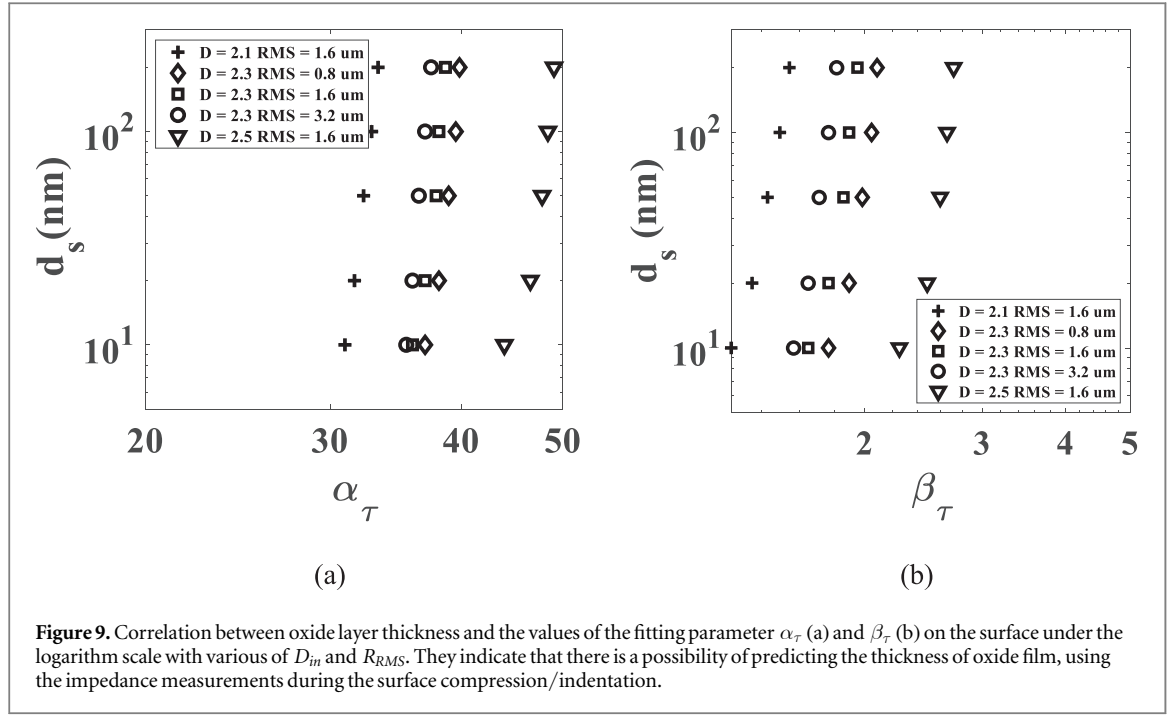
Film thickness (nm)	Coefficient of correlation (for α_τ)	Coefficient of correlation (for β_τ)	R-Square
10	30.82 ± 0.63	1.26 ± 0.04	0.9689
20	32.03 ± 0.23	1.43 ± 0.06	0.9731
50	32.87 ± 0.12	1.54 ± 0.05	0.9675
100	33.66 ± 0.27	1.62 ± 0.08	0.9610
200	34.20 ± 0.48	1.68 ± 0.09	0.9540

neglected, yielding the upper bound characteristic frequency $\tau_\infty = \frac{1}{2\pi\rho\varepsilon_r\varepsilon_0}$, which is determined by the material properties of the oxide layer (ρ , ε_r and ε_0), which can not be used to determine the thickness of the oxide film. Figure 8 shows the performance of characteristic frequency during the initial compression for contacting the fractal rough surface with $FD = 2.1$ and $R_{RMS} = 3.2 \mu\text{m}$ with varying oxide film thickness.

The linear relationship between the characteristic frequency and the applied load in a log-log scale suggests a power-law relationship, which can be described as:

$$\tau = \alpha_\tau \left(\frac{F}{EA} \right)^{\beta_\tau} \quad (21)$$

where the parameter α_τ , β_τ is related to the surface roughness parameters and thickness of the oxide layer. The fitting parameters and the goodness of fitting (R-Square) are reported in table 3 below. Similar to the relationship between ECR and contact force, the format of the power-law relationship (in equation (21)) here can be applied to various conductive materials. However, the particular values of intersect α_τ and



slope β_τ are affected by the mechanical properties of contact material in the contact model.

The predicted oxide layer thickness exhibits a power-law relationship with respect to the fitting parameter β_τ , which can be observed in figure 9. As a result, by employing the power-law correlation between β_τ and oxide film thickness, the oxide layer thickness can be determined from simple measurements of the contact load and characteristic frequency. It worth mentioning that oxide film thickness can be obtained with known surface topology and characteristic frequency variation during the surface indentation and without understanding the correlation between fitting parameters α_τ , β_τ and fractal dimension and R_{RMS} .

4. Conclusions

We performed numerical and theoretical investigations on the stress-dependent impedance at the fractal rough interfaces. The combination of the truncation approach and simulation of interfacial impedance responses at given truncation height enabled the investigation of the stress-dependent impedance behaviour of fractal rough surfaces. Through parametric analyses, the relationships between the fractal dimension, R_{RMS} and oxide layer thickness and the electrical contact resistance, interfacial capacitance and characteristic frequency were established, yielding an explicit expression to describe these relationships. This simple expression provides insights into the estimation of oxide thickness of rough surfaces based on electrical impedance measurements. In view of the demonstrated results and discussion, the following main conclusions can be drawn:

- (1) For various surface structures with the presence of a thin oxide layer, stress-dependent interfacial electrical responses have been observed, manifested in terms of contact resistance, interfacial capacitance and characteristic frequency.
- (2) An analytical model is proposed to investigate the interfacial capacitance with varying contact load, and its validity is verified by the FEM simulation results. The model reveals the predominance of the gap capacitance mechanism under light load, while the interfacial capacitance is dominant by the contact layer capacitance mechanism in large contact load.
- (3) The interfacial capacitance increases with increasing the contact load and decreases with the increase of R_{RMS} . As for the effect of fractal dimension, higher fractal dimension yields smaller capacitance in the gap dominant and transition zone, while the capacitance values are not distinguishable due to the majority of microcontacts are flattened, which are in plastic deformation regime and would be insensitive to surface topography.
- (4) The relationship between characteristic frequency and contact load is examined and can be expressed as a power law. In addition, the parameters β_τ and α_τ show power-law relationships with the thickness of the oxide layer. This implies that impedance measurements during surface contacting can be used to determine the thickness of the oxide layer on the conductive fractal rough surface with known surface topologies.

Acknowledgments

This work was financially supported by The University of Sydney SOAR Fellowship. Mr Xu Wang acknowledges the financial support from the Australian commonwealth government scholarship for conducting his PhD research project at The University of Sydney.


Data availability statement

All data that support the findings of this study are included within the article (and any supplementary files).

ORCID iDs

Xu Wang  <https://orcid.org/0000-0003-3422-1939>

Chongpu Zhai  <https://orcid.org/0000-0002-2849-7894>

Yixiang Gan  <https://orcid.org/0000-0002-9621-0277>

References

- [1] Simon P and Gogotsi Y 2008 Materials for electrochemical capacitors *Nat. Mater.* **7** 845–54
- [2] Abdeljawad F, Völker B, Davis R, McMeeking R M and Haataja M 2014 Connecting microstructural coarsening processes to electrochemical performance in solid oxide fuel cells: An integrated modeling approach *J. Power Sources* **250** 319–31
- [3] Kogut L and Komvopoulos K 2003 Electrical contact resistance theory for conductive rough surfaces *J. Appl. Phys.* **94** 3153–62
- [4] Kogut L and Komvopoulos K 2004 Electrical contact resistance theory for conductive rough surfaces separated by a thin insulating film *J. Appl. Phys.* **95** 576–85
- [5] Zhai C, Hanaor D, Proust G, Brassart L and Gan Y 2016 Interfacial electro-mechanical behaviour at rough surfaces *Extreme Mechanics Letters* **9** 422–9
- [6] Guha K, Kumar M, Agarwal S and Baishya S 2015 A modified capacitance model of RF MEMS shunt switch incorporating fringing field effects of perforated beam *Solid-State Electronics* **114** 35–42
- [7] Ji R, Gao J, Flowers G T, Xie G, Cheng Z and Jin Q 2017 The effect of electrical connector degradation on high-frequency signal transmission *IEEE Trans. Compon. Packag. Technol.* **7** 1163
- [8] Kogut L 2005 The influence of surface topography on the electromechanical characteristics of parallel-plate MEMS capacitors *J. Micromech. Microeng.* **15** 1068
- [9] Yu A, Liu A, Zhang Q and Hosseini H 2006 Effects of surface roughness on electromagnetic characteristics of capacitive switches *J. Micromech. Microeng.* **16** 2157
- [10] Ghandehari M and Sidelev A 2018 Detection of subsurface metal oxidation with thermal imaging *Optical Phenomenology and Applications* (Berlin: Springer) pp 241–52
- [11] Gonzales A and Philofsky E 1971 Applications of scanning electron microscopy to thin film studies on semiconductor devices *Proc. IEEE* **59** 1429–33
- [12] Tai C C, Rose J H and Moulder J C 1996 Thickness and conductivity of metallic layers from pulsed eddy-current measurements *Rev. Sci. Instrum.* **67** 3965–72
- [13] Greenwood J and Williamson J P 1966 Contact of nominally flat surfaces *Proc. R. Soc. Lond. A* **295** 300–19
- [14] Greenwood J A 1966 Constriction resistance and the real area of contact, *British J. Appl. Phys.* **17** 1621
- [15] Wilson W E, Angadi S V and Jackson R L 2010 Surface separation and contact resistance considering sinusoidal elastic-plastic multi-scale rough surface contact *Wear* **268** 190–201
- [16] Paggi M and Barber J 2011 Contact conductance of rough surfaces composed of modified RMD patches *Int. J. Heat Mass Transfer* **54** 4664–72
- [17] Müser M H, Dapp W B, Bugnicourt R, Sainsot P, Lesaffre N, Lubrecht T A, Persson B N, Harris K, Bennett A and Schulze K 2017 Meeting the contact-mechanics challenge *Tribol. Lett.* **65** 118
- [18] Jackson R L and Green I 2005 A finite element study of elasto-plastic hemispherical contact against a rigid flat *J. Tribol.* **127** 343–54
- [19] Pohrt R and Popov V L 2012 Normal contact stiffness of elastic solids with fractal rough surfaces *Phys. Rev. Lett.* **108** 104301
- [20] Pastewka L and Robbins M O 2014 Contact between rough surfaces and a criterion for macroscopic adhesion *Proc. Natl Acad. Sci.* **111** 3298–303
- [21] Murashov M V and Panin S D 2015 Numerical modelling of contact heat transfer problem with work hardened rough surfaces *Int. J. Heat Mass Transfer* **90** 72–80
- [22] Saoudi A, Leon A, Gregoire G, Barasinski A, Djebaili H and Chinesta F 2017 On the interfacial thermal properties of two rough surfaces in contact in preimpregnated composites consolidation *Surface Topography: Metrology and Properties* **5** 045010
- [23] Dervos C T and Michaelides J M 1998 The effect of contact capacitance on current-voltage characteristics of stationary metal contacts *Ieee T Compon Pack A* **21** 530–40
- [24] Zhao Y-P, Wang G-C, Lu T-M, Palasantzas G and De J T M 1999 Hosson, Surface-roughness effect on capacitance and leakage current of an insulating film *Physical review B* **60** 9157
- [25] Patrikar R M 2004 Modeling and simulation of surface roughness *Appl. Surf. Sci.* **228** 213–20
- [26] Chen Z, Tian W and Zhang X 2017 Effect of surface asperities on the capacitances of capacitive RF MEMS switches *J. Micromech. Microeng.* **27** 034002
- [27] Torabi S, Cherry M, Duijnste E A, Le Corre V M, Qiu L, Hummelen J C, Palasantzas G and Koster L J A 2017 Rough Electrode Creates Excess Capacitance in Thin-Film Capacitors *ACS Appl. Mater. Interfaces* **9** 27290–7
- [28] Mandelbrot B B 1983 *The Fractal Geometry of Nature* (New York: WH Freeman) (<https://doi.org/10.1119/1.13295>)
- [29] Kogut L and Etsion I 2004 A static friction model for elastic-plastic contacting rough surfaces *J. Tribol.* **126** 34–40
- [30] Zhai C, Hanaor D and Gan Y 2017 Contact stiffness of multiscale surfaces by truncation analysis *Int. J. Mech. Sci.* **131** 305–16
- [31] Chen J, Lin H, Shen L, He Y, Zhang M and Liao B-Q 2017 Realization of quantifying interfacial interactions between a randomly rough membrane surface and a foulant particle *Bioresour. Technol.* **226** 220–8
- [32] Falconer K 2004 *Fractal Geometry: Mathematical Foundations and Applications* (New York: Wiley) (<https://doi.org/10.1002/0470013850>)
- [33] Zhang X, Xu Y and Jackson R L 2017 An analysis of generated fractal and measured rough surfaces in regards to their multi-scale structure and fractal dimension *Tribol. Int.* **105** 94–101
- [34] Hough S 1989 On the use of spectral methods for the determination of fractal dimension *Geophys. Res. Lett.* **16** 673–6
- [35] Douketis C, Wang Z, Haslett T L and Moskovits M 1995 Fractal character of cold-deposited silver films determined by low-temperature scanning tunneling microscopy *Phys. Rev. B* **51** 11022–31
- [36] Klinkenberg B and Goodchild M 1992 The fractal properties of topography: a comparison of methods *Earth Surf. Processes Landforms* **17** 217–34

- [37] Chen Z, Liu Y and Zhou P 2018 A comparative study of fractal dimension calculation methods for rough surface profiles *Chaos, Solitons Fractals* **112** 24–30
- [38] Fardin N, Stephansson O and Jing L 2001 The scale dependence of rock joint surface roughness *Int. J. Rock Mech. Min. Sci.* **38** 659–69
- [39] Sneddon I N 1965 The relation between load and penetration in the axisymmetric Boussinesq problem for a punch of arbitrary profile *Int. J. Eng. Sci.* **3** 47–57
- [40] Nair M, Guerrero L, Arenas O L and Nair P 1999 Chemically deposited copper oxide thin films: structural, optical and electrical characteristics *Appl. Surf. Sci.* **150** 143–51
- [41] Gattinoni C and Michaelides A 2015 Atomistic details of oxide surfaces and surface oxidation: the example of copper and its oxides *Surf. Sci. Rep.* **70** 424–47
- [42] Bracco G and Holst B 2013 *Surface Science Techniques* (Berlin, Heidelberg: Springer Science & Business Media) (<https://doi.org/10.1007/978-3-642-34243-1>)
- [43] Craig R R 2011 *Mechanics of Materials* 3rd Edn (New York: Wiley, Incorporated)
- [44] Sarkar S, Jana P K, Chaudhuri B and Sakata H 2006 Copper (II) oxide as a giant dielectric material *Appl. Phys. Lett.* **89** 212905
- [45] Matula R A 1979 Electrical resistivity of copper, gold, palladium, and silver *J. Phys. Chem. Ref. Data* **8** 1147–298
- [46] Zhai C, Hanaor D, Proust G and Gan Y 2015 Stress-dependent electrical contact resistance at fractal rough surfaces *J. Eng. Mech.* **143** B4015001
- [47] Prajapati D K and Tiwari M 2019 Investigation on metallic contact conditions using ECR technique by performing rolling/sliding experiments *Surface Topography: Metrology and Properties* **7** 015015
- [48] Pohrt R, Popov V L and Filippov A E 2012 Normal contact stiffness of elastic solids with fractal rough surfaces for one- and three-dimensional systems *Phys. Rev. E* **86** 026710
- [49] Persson B N 2006 Contact mechanics for randomly rough surfaces *Surf. Sci. Rep.* **61** 201–27
- [50] Yang H, Tong Y, Flowers G and Cheng Z 2016 Capacitance build-up in electrical connectors due to vibration induce fretting corrosion, *Electrical Contacts (Holm) 2016 IEEE 62nd Holm Conf. on (Piscataway, NJ)* (IEEE) pp 152–8
- [51] Timsit R S 2005 High speed electronic connectors: a review of electrical contact properties *IEICE Trans. Electron.* **E88-C** 1532–45